



Reduced-order modeling of a bat flying with heavy and highly articulated wings

Xiaozhou Fan* and Kenneth Breuer†

Center of Fluid Mechanics, School of Engineering, Brown University, Providence RI 02912 USA

A three dimensional reduced-order modeling technique is described for modelling both wing inertial and aerodynamic forces found in flapping animals and robots. The model is applied to previously-measured flight of a lesser-nosed dog-faced fruit bat (*Cynopterus brachyotis*) in straight and climbing flight. Quasi-steady Blade Element Momentum Theory (BEMT) is used to model the aerodynamic forces on each segment of the highly articulated wing, and Lagrangian equation of motion is adopted to describe the overall wing-body dynamics that encompasses inertial of wing. When used apart, these two distinct, independent modeling techniques yield excellent agreement in lift generation and matches trend in thrust; if combined, the simulated body trajectories match closely with that of the recorded. First time in our knowledge, the quantitative effect of wing camber was examined, which contributed to 27% of averaged lift, with a smaller price (10%) paid to drag.

Nomenclature

X	=	streamwise direction in global coordinate \mathbf{G}
Y	=	sideslip direction in global coordinate \mathbf{G}
Z	=	vertical direction in global coordinate \mathbf{G}
x	=	thrust direction in body-fixed coordinate \mathbf{B}
y	=	lateral direction in body-fixed coordinate \mathbf{B}
z	=	lift direction in body-fixed coordinate \mathbf{B}
i	=	the index for the wing segment
$\hat{\mathbf{i}}$	=	i -th blade element local streamwise direction
$\hat{\mathbf{j}}$	=	i -th blade element local spanwise direction
$\hat{\mathbf{k}}$	=	i -th blade element local vertical direction
C_l	=	lift coefficient used for each blade element
C_d	=	drag coefficient used for each blade element
C_{rot}	=	rotational lift coefficient used for each blade element
c	=	chord length
f	=	flapping frequency
U	=	magnitude of body velocity
ρ	=	air density
α	=	effective angle of attack
α_0	=	zero lift angle of attack

I. Introduction

Research in flapping wing flight has advanced dramatically over the two decades [1]. Studies on various sizes of animals such as the bumblebee (*Bombus impatiens*) [2], the desert locust (*Schistocerca gregaria*) [3], the hawkmoth (*Manduca*) [4], the painted lady butterfly (*Vanessa cardui*) [5] and the fruit fly (*Drosophila*) [6] has revealed the important effects of wing kinematics to the formation and breakdown of the leading edge vortex (LEV). Larger animals such as the thrush nightingale (*Luscinia luscinia L*) [7] and rock pigeon [8–10] reveals additional features that birds exhibit with their more flexible and articulated wing structure. For example, during upstroke, birds actively fold their wings to

*Graduate Research Assistant

†Professor, AIAA Associate Fellow

reduce the wetted surface area and in this way minimize negative lift generated [9, 11, 12]. Through experiment methods such as PIV measurements [13–15], it is revealed that bats accentuate these additional degrees of flight complexity, with their highly articulated membrane wings which contribute to bats’ extreme flight maneuverability and agility.

Quantitative modelling and simulation of flapping flight and, more recently, robotic flight has also grown in the past few decades. Although large-scale unsteady computational fluid dynamic (CFD) simulations have revealed many important complex flow features associated with flapping flight [12, 16–18], reduced-order modelling (ROM) [6, 19–21] has certain advantages over CFD as being much cheaper in terms of both computational resources and time needed, while maintaining first-order physics.

To be successful, however, ROM must capture both the aerodynamic and the inertial contributions to flapping flight. Blade Element Momentum Theory (BEMT) [22, 23] has been developed into an invaluable tool for estimating the aerodynamic forces associated with animal wing motions [24, 25]. However, quite a few studies [19, 20, 23, 26, 27] would first define a stroke plane, based on which the flapping angle, stroke plane deviation and wing rotation are then introduced. Other studies would bypass the stroke plane by imposing either a functional form (e.g., harmonic function \sin) to the wing kinematics [9, 10, 28] or a linear angle variation along the span by a representative anatomy location extracted from measurement (e.g., the wrist location in [24] or the wing tip in [27]).

These approaches are arguably suitable for an insect wing, where the deformation of wing geometry is relatively small and a characteristic marker to define the stroke plane is clear, and the linear assumption might hold. However, for a highly-articulated bat wing, the kinematic and geometric variation along span is much more pronounced and highly nonlinear, and this yields an ill-defined stroke plane [27]. Since the kinematics of each blade element is of paramount importance and the ensuing the aerodynamics are contingent on it, an over-simplification of kinematics might miss critical features such as the effective angle of attack or the segment velocity. Moreover, although CFD studies have identified the importance of wing camber on aerodynamics [3–5, 27, 29] or fluid-structure interaction studies [30], there has yet to be a ROM study on animal flight that incorporates camber in the aerodynamic model.

The importance of inertial effects of wing motion on overall flight dynamics has also been shown to be critical, particularly in the case of bats who have relatively large fractions of their body mass distributed in their wings [11, 31]. For these animals, accelerating heavy wings requires additional forces and torques and any ROM that hopes to address flight power requirements must account for wing mass which, due to complex wing articulation, can re-distribute and re-orient during the wingbeat cycle. Finally, the body acceleration (“recoil”) due to heavy wing motion is substantial [21, 32–34], and is largely omitted in the studies concerning animal flight [24, 27].

The present manuscript attempts to address these shortcomings and demonstrates progress towards the development of a three-dimensional, low-order model, to simulate aerodynamic and inertial forces associated with flapping flight of animals and/or robotic flight vehicles that are characterized by highly articulated, flexible thin wings. We introduce a new technique to directly discretize the complicated, deforming bat wing into a set of wing segments, where each segment includes camber and, with six degrees of freedom, is capable of representing complex segment-wise kinematics with high-fidelity. The model employs Blade Element Momentum Theory, including the wake effect (i.e. the induced angle-of-attack) to estimate aerodynamic forces; the time-varying distribution of wing mass is also accounted for, allowing us to simulate the body recoil motion due to the highly articulated, massive wings.

In this manuscript we describe the development of the model, and validate our approach using previously-measured wing and body kinematics of a fruit bat, *Cynopterus brachyotis*, recorded in a wind tunnel environment [35].

II. Methods

A. Experimental Data

The kinematics analysed in this manuscript are derived from previously reported measurements of the flight in a wind tunnel of the lesser-nosed dog-faced fruit bat, *Cynopterus brachyotis* [11, 35]. These animals are medium-sized fruit bats, weighing about ~ 34 grams. They typically have a wingspan of approximately 36 cm, and an average chord $c = 6$ cm, which yields an aspect ratio 6 and maximum wing area of ~ 0.25 m². The experimentally recorded flight speeds range from 3.25 to 7.43 m/s. In this manuscript, we focus on a single flight in which the net airspeed of the bat was $U = 4.75 \pm 0.20$ m/s. The chord Reynolds number $Re = Uc/\nu$ was 15,700 and the Strouhal number, $St = fh_a/U$, was ≈ 0.4 , where ν is the kinematic viscosity of air, the flapping frequency, $f = 9.57$ Hz, and the wing beat amplitude, $h_a = 0.2$ m.

As seen in Fig. 1a, The wing and body kinematics were determined from 3D stereo tracking of markers placed on around 50 anatomical locations on the animal’s trunk and left wing, and recorded at 1000 frames per second; the time

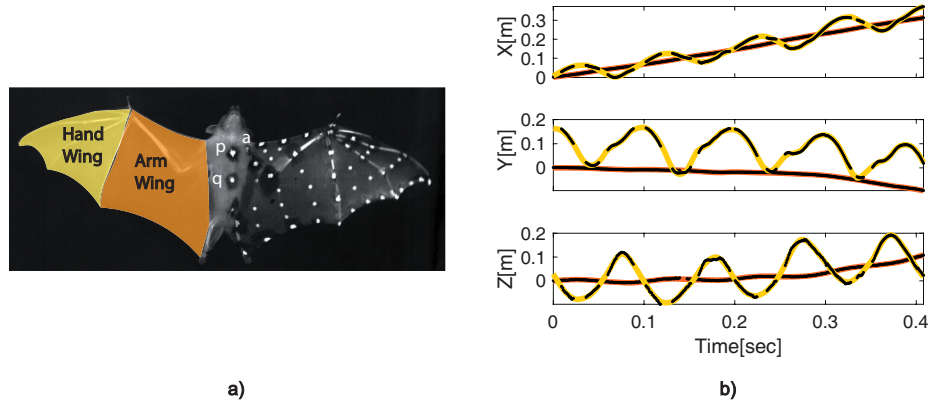


Fig. 1 Marker patterns and data conditioning. a) "p"(sternum), "q"(lumbar) and "a"(shoulder) are three markers selected to construct the body-fixed coordinate \mathbf{B} , in which an arm wing (orange) and a hand wing (gold) will be analyzed in detail. b) The imputed X -, Y - and Z - (black line) coordinates from sternum (orange) and wing tip (gold) are presented, and raw data (black lines) are presented.

duration of this flight was around 0.4 seconds. The flight was nearly left-right symmetric, and so, by assuming that the right wing motion is the mirror-image of the left wing, a complete model of the body kinematics could be generated.

The wing motion of bats is complex, and the tracked locations of wing markers were interpolated and filtered using imputation [36] to address the occasional occlusion and digitizing noise present in the dataset (Fig. 1b). Trimmed Score Regression (TSR) not only infers the position of occluded markers, but also filters noise stemming from stereo triangulation. This technique takes consideration of the temporal evolution of a marker, as well as the spatial information, such as the relative locus of neighborhood markers. Note that wing tip marker (gold in Fig. 1a) has more occlusion than the body marker (orange) as a result of insufficient camera observation (< 2) to perform accurate stereo triangulation. The raw data (black) is first detrended and normalized, which helps TSR equally weight markers with either large (e.g. wing tip) or small (e.g., body markers) oscillatory motions.

A global inertial coordinate system \mathbf{G} was defined (Fig. 2a). The X -axis points in the streamwise direction of the wind tunnel, and the Z -axis is vertical, pointing upward towards the ceiling of the tunnel. The Y -axis could then be determined by the right hand rule. As seen in Fig. 1a, the sternum marker (labeled "p") was chosen to be the origin of the body-fixed coordinate, \mathbf{B} . The lumbar-sternum vector (in Fig. 1a, "q-p") is the heading (x -axis) of \mathbf{B} , and the y -axis of \mathbf{B} is the surface normal of the triangle "a-p-q", where "a" is the left shoulder marker. The z -axis then follows the right hand rule. As seen in Fig. 2a, the origin of the body-fixed coordinate, \mathbf{B} , travels with the bat in three translational directions and undergoes three consecutive Euler rotations as Yaw (ψ_b) - Roll (ϕ_b) - Pitch (θ_b).

The X , Y and Z coordinates of the sternum marker in \mathbf{G} were given in Fig. 2b, along with the three Euler angles associated with the orientation of the body. Time is non-dimensionalized by the duration of the average wingbeat period which, for this trial was three complete flapping cycles. The grey shaded area represent the downstroke identified by the peaks and troughs of the z component of the shoulder marker in \mathbf{B} . The duration of downstroke lasts slightly longer than that of the upstroke. This flight is predominantly straight with a gentle climb, as evidently supported by the X and Z in Fig. 2b. There is minimum body roll and yaw (both are ~ 5 degree over the course of flight). The body pitch fluctuates around -10 to -20 degrees, and the nose-up motion happens mainly in downstroke. In the global coordinate \mathbf{G} , the bat travels forward (X direction) for about 2 meter with a climbing height (Z direction) of about 20 centimeter. The sideslip (Y direction) is rather small (~ 3 centimeter.)

B. Wing Kinematics and Camber

To model both inertial and aerodynamic measurements, the wing is segmented into a series of discrete blade elements [22]. The wing was divided into $N = 10$ segments, as the number of segments is shown to have only marginal effect on the aerodynamic calculations for $N > 10$. Concretely in Fig. 3a, the span line, defined as a curve (purple "QC") that connects the quarter-chord of all the segments is derived from the leading and trailing edge lines ("LE" and "TE" respectively). It determines the three translational DoFs in \mathbf{B} (x_i, y_i, z_i) for the i -th segment. To define the rotational DoFs, the bearing of each segment is constructed as a line from the TE to LE; then the span direction of each segment is

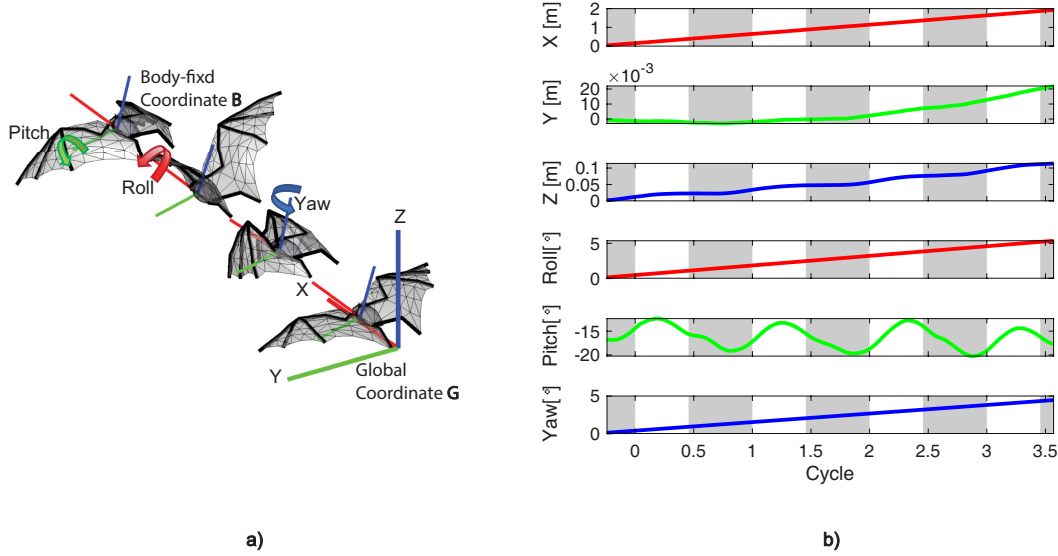


Fig. 2 Global coordinate, \mathbf{G} and body-fixed coordinate, \mathbf{B} . a) The body has 6 degree of freedom (DoF) in \mathbf{G} : 3 translational DoFs (X , Y and Z), and 3 consecutive Euler rotations: Yaw, Roll and Pitch. b), Quantitative description of the 6 DoFs of body in \mathbf{G} . Grey shades indicate downstroke.

defined as the vector direction tangent to the span line (“QC”). The third axis (segment surface normal) then follows the right hand rule. The three Euler angles for the i -th segment (yaw - roll - pitch) can thus be calculated. In other words, for the i -th blade element, it is defined uniquely by the quarter-chord location relative to the origin of the body-fixed coordinate \mathbf{B} , (x_i, y_i, z_i) , as well as the element orientation, defined by Euler angles, ϕ_i, ψ_i, θ_i , again, with reference to the body-fixed coordinate system, \mathbf{B} . In general, as shown in Fig.3b, the segment in the distal part of the wing (the “hand wing”) exhibits more pronounced oscillatory motion than the proximal segment (the “arm wing”), as the excursions of the the hand wing segment (gold) are larger than these of the arm wing segment (orange) in all directions. The relative motion between the two segments can be readily extended to understand the motion of hand and arm wing as well, where the difference in y reflects the wing folding, and that the difference in pitching angles is due to the wing twist along the span. Interestingly, both the hand and arm wing orient similarly during downstroke, but differ greatly during upstroke, when the hand wing starts to thrust forward (yaws as large as -100°) and pitches up (also around -100°). This combined rotation results in the hand wing being almost perpendicular to the floor, with the left and right palms facing each other. This articulation greatly reduces the wetted surface area seen by the incoming flow, which ultimately translates to a reduction in negative lift during the upstroke.

C. Camber

We model the geometry of each blade element as a two-dimensional thin airfoil with camber. The angle of attack and camber are calculated by fitting Fourier series to the measured data, and using thin airfoil theory to associate the Fourier coefficients with the camber of the airfoil[37]. The camber ultimately translates to a zero-lift angle of attack, α_0 . Specifically, at each time, t_k , a Delaunay triangulation is performed on the wing marker distribution. This mesh structure pierces the vertical segment plane forming a set of points that describe the wing surface in segment plane (Fig. 4a, black dots). These points are fitted, in the least-squared error sense, with the first two modes of a Fourier Sine series (Fig. 4b). The coefficients of these modes are directly related to the zero lift angle of attack α_0 [37]. The first mode (blue) captures the angle of incidence in the local segment axes, and the second mode (green) relates the camber, the combination of which yield the cambered segment (red).

Both the hand and arm wing start with little or no camber at the beginning of downstroke, and become more bulged towards the end of downstroke due to the aerodynamic loading, reaching about 10% of the chord (Fig. 5a). Interestingly for the arm wing, even during upstroke, the camber of the arm wing continues to grow due to the combined motion of legs and elbows, and peaks ($\sim 15\%$ of the chord) at late upstroke, before it drops precipitously as the legs swing back and upward to align with the body. For the hand wing, however, the digits curl inward at the onset of the upstroke but the

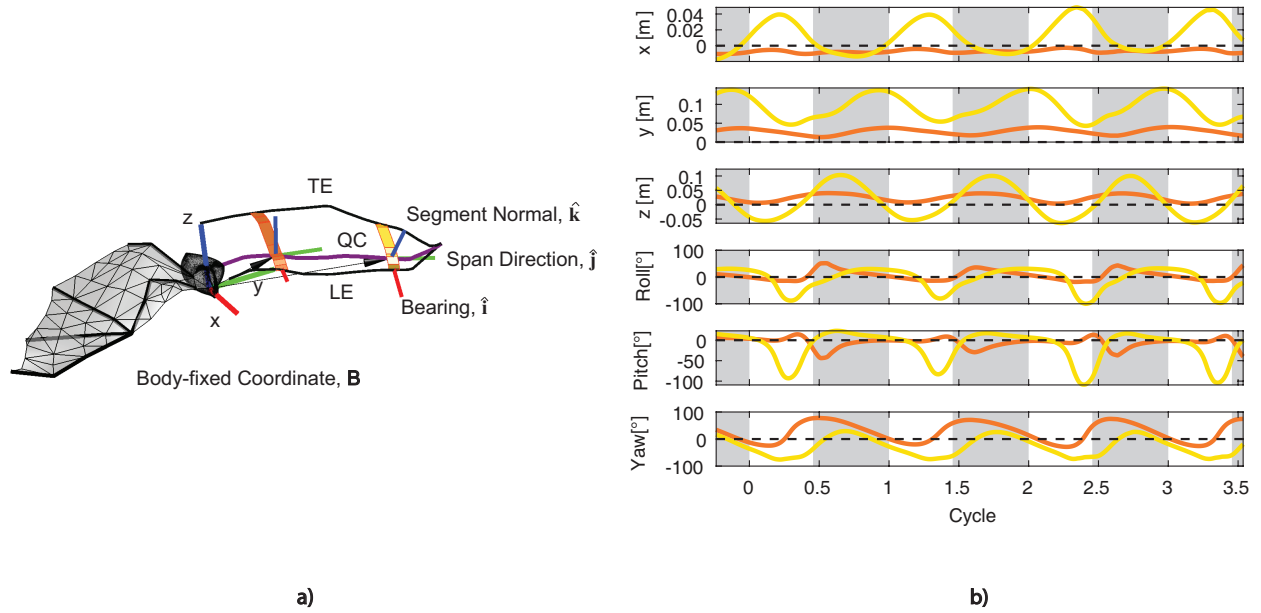


Fig. 3 Segment kinematics in B. a) Two segments are selected to represent arm and hand wing kinematics, each having its own local axes. b) Quantitative description of 6 DoF evolution for hand (1/4 span, in orange) and arm (3/4 span, in gold) wing. The grey shades indicate downstroke.

camber decreases sharply towards the end of upstroke, when the fingers start to spread outward and prepare for the next downstroke.

D. Blade Element Momentum Theory

Blade element theory [6, 9, 10, 20, 22, 38] is used to model the aerodynamic forces generated by the wings. For the i -th blade element, the total force, $\Delta \mathbf{F}_i$, has two components:

$$\Delta \mathbf{F}_i = \Delta \mathbf{F}_{\text{trans},i} + \Delta \mathbf{F}_{\text{rot},i}, \quad (1)$$

where $\Delta \mathbf{F}_{\text{trans},i}$ is the aerodynamic force due to the translational motion of the wing, while $\Delta \mathbf{F}_{\text{rot},i}$ corresponds to the force generated by the wing rotation [38, 39]. Furthermore, we can separate the translational force in terms of lift and

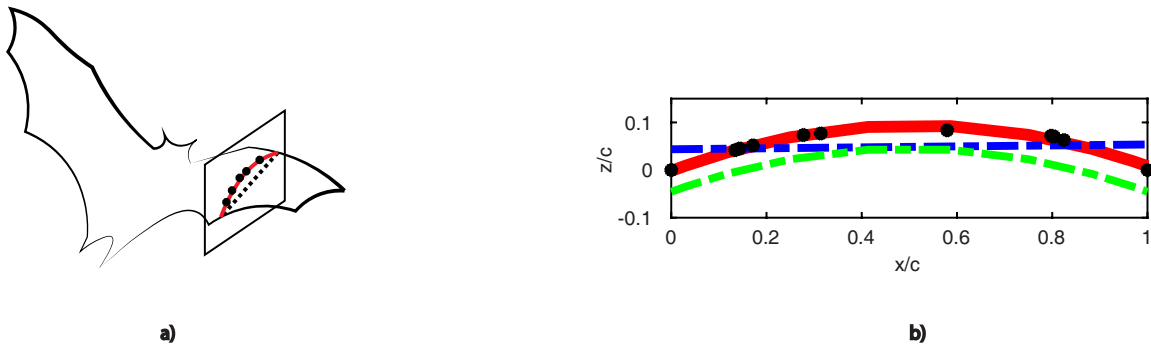


Fig. 4 Camber of the membrane wing due to aerodynamic and wing inertial forces. a) The vertical segment plane intersects the surface mesh generated by the experimental markers. b) The first mode (blue), second mode (green) and the sum of the two modes (red) from the Fourier series are fitted to the raw data (black dots) to represent camber in the local segment axes.

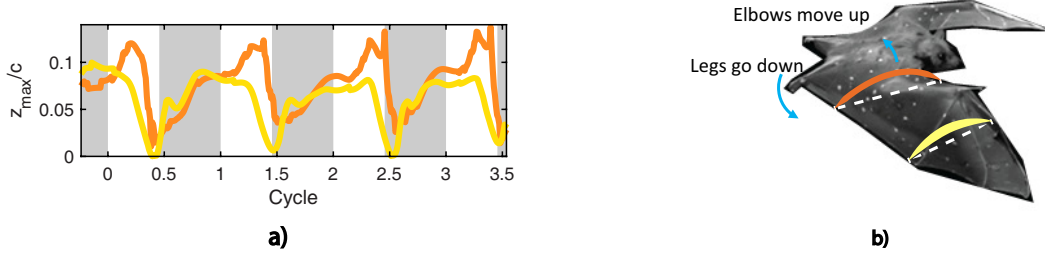


Fig. 5 The time evolution of camber and the mechanics explained. a) The nondimensionalized camber for arm wing (orange) and the hand wing (gold). The grey shades indicate downstroke. b) The mechanics of camber is different for arm and hand wing. For the arm wing, the legs control the ventral-dorsal movement of the trailing edge while the elbow moves out of phase of leg to yield the camber.

drag:

$$\Delta \mathbf{F}_{\text{trans},i} = \Delta \mathbf{L}_i + \Delta \mathbf{D}_i, \quad (2)$$

where the segment-wise lift $\Delta \mathbf{L}_i$ and drag $\Delta \mathbf{D}_i$ are then given as:

$$\Delta \mathbf{L}_i = 1/2 \rho c_i \Delta r_i C_l |\mathbf{U}_i| (\mathbf{U}_i \times \hat{\mathbf{j}}) \quad (3)$$

$$\Delta \mathbf{D}_i = -1/2 \rho c_i \Delta r_i C_d |\mathbf{U}_i| \mathbf{U}_i, \quad (4)$$

where ρ , c_i , Δr_i and \mathbf{U}_i are the air density, chord length, width, and velocity vector of the i -th segment in the global coordinate system \mathbf{G} . Due to the highly-articulated nature of the bat wing, both c_i and Δr_i vary with time as the result of the wing extending and retracting. The unit vector $\hat{\mathbf{j}}$ is the segment spanwise direction (Fig. 2a). The lift and drag on each segment are assumed to be located at the quarter-chord position of the segment. Finally, the aerodynamic coefficients used in the lift (C_l) and drag (C_d) are taken as:

$$C_l = A \sin(2(\alpha - \alpha_0)) \quad (5)$$

$$C_d = B - C \cos(2(\alpha - \alpha_0)), \quad (6)$$

where A, B and C are empirical constants derived from experiments [9, 40], and α , α_0 are the effective and zero-lift angle of attack for this segment respectively.

The rotational component of the aerodynamic force $\Delta \mathbf{F}_{\text{rot},i}$, is given by [20, 38]:

$$\Delta \mathbf{F}_{\text{rot},i} = C_{\text{rot}} \rho c_i^2 \dot{\theta}_i |\mathbf{U}_i| \Delta r_i \hat{\mathbf{k}}, \quad (7)$$

where the rotational force coefficient, C_{rot} , is given by $C_{\text{rot}} = \pi(0.75 - x/c)$, and $x/c = 0$ and 1 refer to the leading and trailing edge respectively [39]. For simplicity, we assuming that the pitching axis is the quarter-chord location. $\dot{\theta}_i$ is the angular pitching velocity and the unit vector, $\hat{\mathbf{k}}$, is the segment normal direction (Fig. 2a). One thing important to mention is that, the velocity, \mathbf{U}_i , refers to the component in the plane of the wing segment (spanned by $\hat{\mathbf{k}} - \hat{\mathbf{i}}$, Fig. 2a).

The geometric angle of attack of each blade element can be calculated from the orientation and velocity of the element with respect to the animal's body in \mathbf{B} , combined with the orientation and velocity of the animal in \mathbf{G} . Afterwards, an induced velocity field is imposed in \mathbf{G} to fully yield the effective angle of attack for each segment [9, 10, 21, 22]. Similar to a fixed-wing of finite wing length, the induced velocity field reduces the angle of attack as evident in Fig. 6, where the cases with wake model (dashed lines) all fall short of those without (solid lines) for both hand (gold) and arm (orange) wings. The effect is more prominent for the arm wing during the downstroke (as much as 10 degrees). During the upstroke, the induced velocity is small and has minimal effect on the angle of attack. Note that the fast pronation of the hand wing (large pitching in Fig. 3b) recovers the effective angle of attack from negative to positive around the beginning of the downstroke.

E. Wing Inertia

Bats, unlike insects and many birds, have relatively heavy wings due to the distribution of heavy bone and muscle within the wing structure. *Cynopterus brachyotis* contains around 21% of its total body mass in the wings [11] and

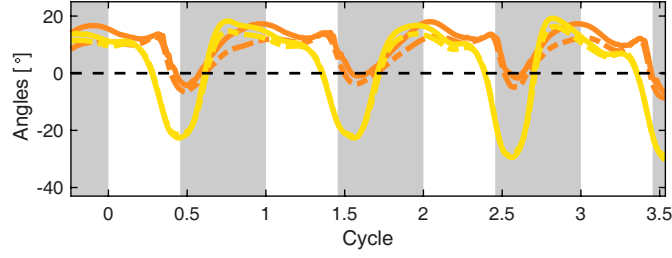


Fig. 6 Effective angle of attack for hand (gold) and arm (orange) wing. The wake model (dashed line) reduces the geometric angle of attack (solid lines) for both hand and arm wings. The grey shades indicate downstroke.

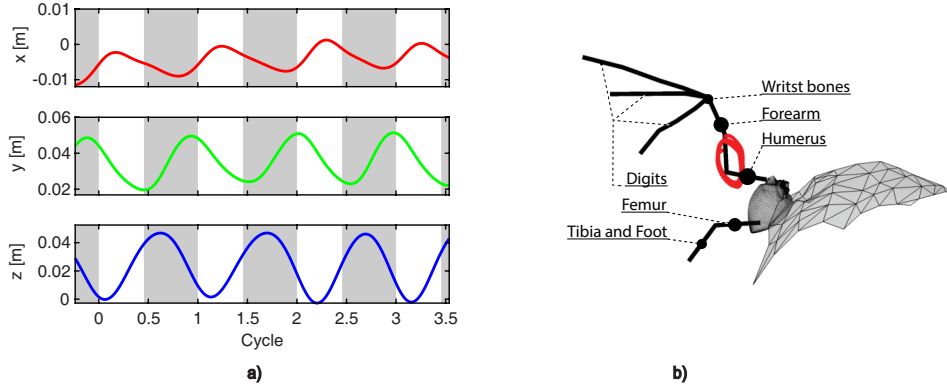


Fig. 7 Wing center of mass (WCoM). **a)** The x -, y - and z - location of WCoM is tracked in body-fixed coordinate **B**. **b)** 3D view of WCoM trajectories (red). The relative weight of bones are indicated by size of the filled black circles[11]. The excursions of the WCoM remain relatively compact and localized.

it is well-established that the motion of the heavy wings affect the overall body dynamics during both steady and maneuvering flight [11, 41]. The accelerations associated with flapping and folding of the wings during flight requires considerable force, and this must be incorporated into the dynamical model so that the total wing-body interaction are accurately captured.

Figure 7 shows the motion of the wing center of mass (WCoM) in **B**. The x -, y - and z -location of wing center of mass, $[x_w, y_w, z_w]^T$, is the weighted average over all the the wing mass distribution (primarily the bones [11]). The fact that the bones contribute to most of the wing mass, and that the proximal bones (humerus, forearm, wrist bones as well as femur, tibia and foot in Fig. 7b) are heavier than distal ones (phalanges, or digits), means that the WCoM should remain close to the body. Over the duration of the wingbeat cycle, the WCoM forms a tight and stable elliptical trajectory in **B** (Fig. 7b). Even though the bat is seen to climb slightly in **G**, the WCoM trajectory stays unchanged, which hints that the bat achieves this control using finer, localized tuning in the light-weighted wing extremities, rather than the heavy bones near the body.

The distribution of the wing mass also defines wing moments of inertia. Concretely, in the body-fixed frame **B**, we define the I_{ij} ($i, j = 1, 2, 3$ for x, y, z) component of the inertia dyadic as:

$$I_{ij} \stackrel{\text{def}}{=} \sum_{k=1}^{N_k} m_k \left(\|\mathbf{r}_k\|^2 \delta_{ij} - x_i^{(k)} x_j^{(k)} \right), \quad (8)$$

where $k = 1 \dots N_k$ identifies each bone and $\mathbf{r}_k = (x_1^{(k)}, x_2^{(k)}, x_3^{(k)})$ is the distance of k -th bone mass to the wing center of mass $[x_w, y_w, z_w]^T$, and δ_{ij} is the kronecker delta. Subsequently, the symmetric and positive definite tensor I_{ij} can be expressed in principal axes and values as $\mathbf{I} = \mathbf{Q}\mathbf{\Lambda}\mathbf{Q}^T$, where the diagonal matrix $\mathbf{\Lambda}$ represents the principal moment of inertia, I_{xx} , I_{yy} and I_{zz} , and the principal axes, \mathbf{Q} , can be further decomposed by a set of consecutive Euler angles, (Yaw(ψ_w) – Roll(ϕ_w) – Pitch(θ_w)) as $\mathbf{Q} = \mathbf{R}(\theta_w)\mathbf{R}(\phi_w)\mathbf{R}(\psi_w)$. $\mathbf{R}(\cdot)$ here is the rotational matrix.

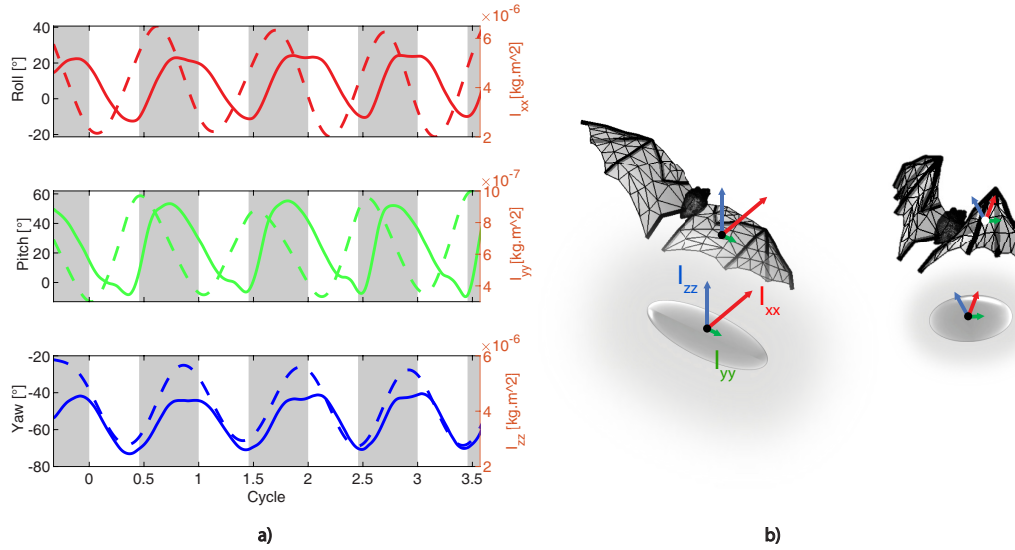


Fig. 8 Principal moment of inertia of the bat wing in body-fixed coordinate **B**. a) The three sequential Euler angles (Yaw - Roll - Pitch) is used to describe the orientation of the principal direction (solid lines) and the magnitude of each component (dashed lines). b) Two typical snapshots in the downstroke and upstroke. The effect of moment of inertia resembles that an expanding and shrinking ellipsoid.

In Fig. 8a, I_{xx} , which is relevant for the flapping motion, is the largest, followed by I_{yy} , which associates with the sweeping motion; finally I_{zz} is the smallest, which resists the wing rotation along the span. For the case of a rigid wing, the direction of the three principal axes vary in **B**, but the magnitude of each component stays the same. Due to the articulation of the wing, however, the magnitudes of the three principal axes ($|I_{xx}|$, $|I_{yy}|$ and $|I_{zz}|$) for the bat wing will also change (Fig. 8b).

It is noted that the for each wing, the wing center of mass as well as the wing moment of inertia is assembled to represent the degrees of freedom for the left and right wings, \mathbf{q}_{lw} and \mathbf{q}_{rw} . For example, for the left wing, $\mathbf{q}_{lw} = [x_{lw}, y_{lw}, z_{lw}, \psi_{lw}, \phi_{lw}, \theta_{lw}]^T$

F. Lagrangian Equation of Motion

In order to model the overall motion of the animal, we write the Lagrangian equation of motion of the three-point-mass system in the global coordinate system **G**:

$$\mathbf{D}(\mathbf{q})\ddot{\mathbf{q}} + \mathbf{C}(\mathbf{q}, \dot{\mathbf{q}})\dot{\mathbf{q}} + \mathbf{g}(\mathbf{q}) = \boldsymbol{\tau} + \mathbf{f}_{\text{aero}}, \quad (9)$$

where the generalized coordinate \mathbf{q} has 18 components (6 DoF for the body, and two 6 DoF for each wing). $\mathbf{D}(\mathbf{q})$, $\mathbf{C}(\mathbf{q}, \dot{\mathbf{q}})$ and $\mathbf{g}(\mathbf{q})$ are the mass matrix, centrifugal matrix and gravitational vector respectively. The generalized torque, $\boldsymbol{\tau} = [0_{1 \times 6}, \tau_{lw, \text{int}}, \tau_{rw, \text{int}}]^T$ denotes the internal forces between the left, right and the body, while \mathbf{f}_{aero} represents the external aerodynamic forces and the ensuing torques felt by both left and right wing. Here, since \mathbf{q} and its derivatives are known from the experimentally measured kinematics, we can directly solve for the x -, y - and z - components of \mathbf{F} . The resulting constraint force is the aerodynamic force that is required for the animal to follow the observed flight path.

A second, independent calculation is to compute the aerodynamic forces from the observed wing kinematics and use those to predict the overall body motion. To this end, at each time t_k , we can rewrite eqn. (9) as:

$$\mathbf{D}(\mathbf{q})\ddot{\mathbf{q}} = \boldsymbol{\tau} + \mathbf{f}_{\text{aero}} - (\mathbf{C}(\mathbf{q}, \dot{\mathbf{q}})\dot{\mathbf{q}} + \mathbf{g}(\mathbf{q})), \quad (10)$$

where the known quantities are \mathbf{q} , $\dot{\mathbf{q}}$ and all the system matrices: $\mathbf{D}(\mathbf{q})$, $\mathbf{C}(\mathbf{q}, \dot{\mathbf{q}})$ and $\mathbf{g}(\mathbf{q})$. We then apply the blade element momentum theory to model the aerodynamics and its ensuing internal torques, \mathbf{f}_{aero} and $\boldsymbol{\tau}$. Thus, eq. (10) becomes a linear system (in the form $\mathbf{Ax} = \mathbf{b}$) at each time t_k , which we can solve for the acceleration of the generalized coordinate $\ddot{\mathbf{q}}$. We can integrate $\ddot{\mathbf{q}}$ to obtain \mathbf{q} , $\dot{\mathbf{q}}$ at the next time, t_{k+1} . In this way, the problem becomes an initial value problem, where the initial conditions at t_o are provided by the measured state of the animal at the start of the recorded kinematics.

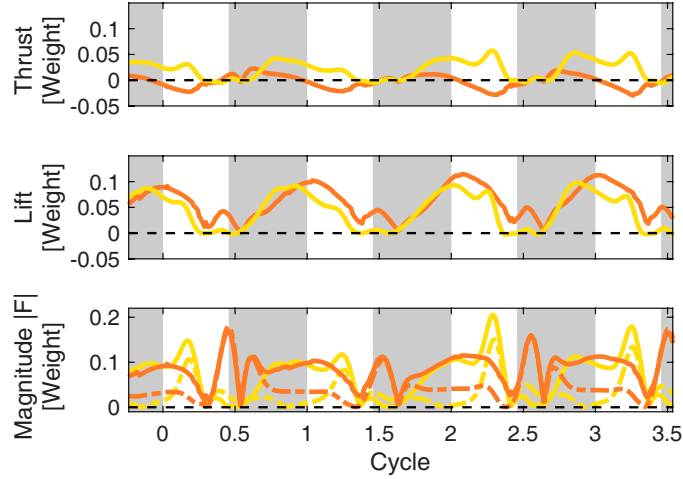


Fig. 9 Aerodynamics of hand (gold) and arm (orange) wings in body-fixed frame **B**. The forces are all normalized by weight of the bat. Rotational lift magnitudes (dash lines) are compared with the total force magnitudes (solid lines). The grey shades represent the downstroke.

G. Error Estimation: Monte Carlo Simulations

The predictions are sensitive to numerous potential errors, primarily associated with uncertainties in the marker location due to stereo triangulation error, in the wind tunnel speed, as well as modelling errors in the constants A , B and C in the aerodynamic model (eq. 5). We quantify the effects of this uncertainty by means of Monte Carlo simulations. For each marker position, a sampling with a mean and a standard deviation of 0.05 cm[35] was taken. Similarly the wind tunnel mean flow was assumed to have an uncertainty of ± 0.2 m/s [35]; the modelling constants, A , B and C , were assigned a standard deviation of 2%. We ran the simulation 20 times, using kinematics and operating conditions sampled from within these uncertainties, and generated average and standard deviations for each computed quantity reported.

III. Results and Discussion

A. Arm and Hand Wing Aerodynamics

Hand and arm produce distinctive aerodynamic signatures (Fig. 9). The hand wing produces most of the positive thrust during both the down- and up-stroke, while both arm and hand wing contribute to lift. It also becomes clear that the rotational component of the aerodynamic force, due to the rapid pitching of hand wing during the upstroke (Fig. 3b), creates local thrust peaks in the middle of upstroke, and that the rotation of the arm wing contributes to positive lift even during the upstroke. Similar trend has also been observed by Song[20] *et al.* in their study of a hovering hummingbird using a blade element analysis. This also agrees with results from PIV measurements by Hubel[14] *et al.*, where they used individuals from the same bat species (*Cynopterus brachyotis*) and found that a vortex pair associated with the arm wing contributes to positive lift. Hedenstrom[13] *et al.* arrived at a similar conclusion from measurements obtained with a different bat species, *Glossophaga soricina*. Furthermore, the fact that hand and arm wing have similar and distinctive roles in lift/thrust generation might suggest a need to model them separately as opposed to lump into one part[21, 42].

B. Comparison of Aerodynamic Forces

The predictions of the two distinctive and independent methods used to model the flight mechanics - blade element momentum theory (BEMT) and Lagrangian equation of motion (LEoM) - are compared in Fig. 10; the cycle-averaged values of lift and thrust are presented in Table 1 in **G**, where the sideslip force (F_y) is left out as the fluctuation is small due to the left-right symmetric condition in **B** imposed. The average thrust/drag should be zero for a self-propelled free flight and, while BEMT under-predicts the average thrust compared to LEoM, both are very small in magnitude and the peaks and troughs align remarkably well. Considering that the BEMT assumes a quasi-steady aerodynamic model that carries no knowledge of the unsteady leading edge vortex (LEV) formation and shedding, this level of agreement is

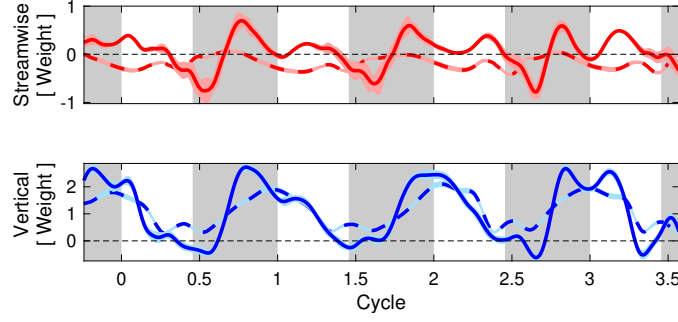


Fig. 10 Comparison of aerodynamics forces from two approaches: the blade element momentum theory (dashed lines) and the Lagrangian equation of motion (solid lines). The errorbar reflects the impact of uncertainties in the experiment. The grey shades represent the downstroke.

quite satisfactory.

For the lift force, both average and instantaneous values predicted by the two schemes match very well and show lift support ($F_z \sim 1$ [Weight]), even corroborating the fact that the bat is climbing gently during this trial. The role of rotational lift clearly kicks in nearing the stroke reversal, when a local peak appears in Fig. 10 at around Cycle = 1.5 and 2.5 for both lagEoM and BEMT. In addition, both models predict either a small negative (LEoM) or even positive lift (BEMT) during upstroke, which align with a recent CFD study of another insectivorous bat in straight flight[12].

Table 1 Cycle-averaged Forces [Weight]

	Lagrangian Equation of Motion	Blade Element Moment Theory
F_x	0.05	-0.16
F_z	1.11	1.10

C. Effect of Camber on Aerodynamics

While reduced-order models presented by other groups have treated the wing as a flat plate at angle of attack, we have incorporated wing camber into our modelling - a feature that is particularly important for the compliant membrane wings that are unique to bat flight. An interesting question is how the cambered wing affects the subsequent aerodynamics. Here, we compare the current results with a case where the camber mode in the Thin Airfoil Fourier series (mode 2 in Fig. 4) is omitted. As seen in Fig. 11, the lift falls when the camber is prominent (late downstroke and early upstroke) as a result of smaller C_L coefficients. The thrust at the same time increases mainly due to the induced lift having a smaller negative projection in the thrust direction, as well as the reduction of C_D . Overall, the cambered wing increases the cycle-averaged lift about 0.27 of the unit weight, while acts to decrease the thrust by 0.1 of the unit weight. Indeed, Gopalakrishnan[29], through CFD simulation, reveals that the LEV tends to “glide” over the camber wing and stays longer in the upper surface than it would for rigid wings, which boosts both lift and thrust generation. Though BEMT assumes a quasi-steady state, the models for C_l and C_d are able to capture some of the unsteady behavior due to the LEV which provide the boost in lift generation. The cycle averaged values are $[F_x, F_z] = [-0.07, 0.84]$ for no camber and $[-0.16, 1.10]$ for the native kinematics.

D. Simulated and Observed Body Trajectories

As mentioned earlier, to simulate the evolution of body trajectories, the observed wing kinematics in **B** is used as input, and drive the body forward. Specifically, the acceleration of body position and orientation are solved and integrated over time. This approach improves on the approach reported by Windes [12]*et al.* in that not only the aerodynamics but also the wing inertia is considered, and that not only body position but also orientation is computed and compared with observed trajectories. As seen in Fig. 12, the comparison between the simulated and observed

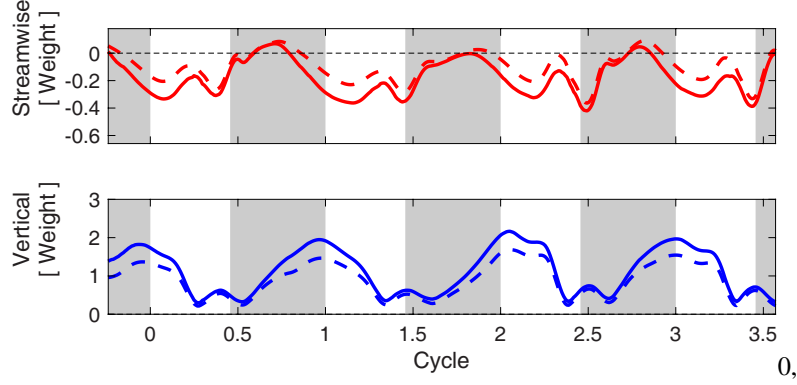


Fig. 11 The effect of camber on the aerodynamic performance. The forces generated by the measured cambered wing (solid line) is compared with a hypothetical case (dashed line) where the second mode of Fourier series, representing camber, is excluded. The grey shades represent the downstroke.

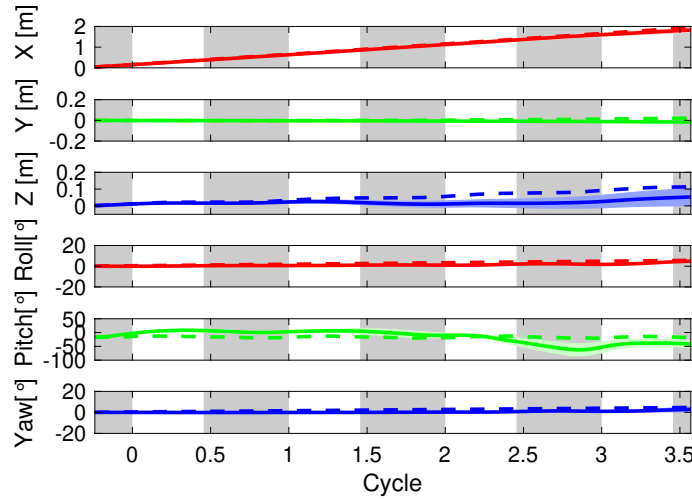


Fig. 12 Comparison of observed (dashed line) and simulated (solid line) body kinematics for 6 DoF in G. The grey shades represent the downstroke.

trajectories is very good in X, Y , roll and yaw (though roll and yaw in this particular flight are both quite small). Particularly, compared to the approach where wing mass is ignored [12], the current method demonstrates much better agreement in the streamwise direction X . The simulation slightly under-predicts the vertical (Z) motion, although is successful in capturing the climbing trend. The simulated pitch motion of the body is seen to oscillate around the observed kinematics. Nevertheless, the overall agreement is very encouraging given the fact that the simulation only uses the left wing kinematics, while the true experiment was not perfectly left-right symmetric.

IV. Conclusion and future work

We have demonstrated the successful development of a reduced-order model capable of both modelling and simulating the flight of a highly-articulated flapping wing systems characteristic of bats and birds, as well as man-made robotic flight vehicles. At this time, all of the components of the analysis tool have been successfully implemented including the calculation of aerodynamic and inertial forces and torques associated with flapping, heavy wings, as well as the resultant, unconstrained, motion of the animal's body due to the net action of those forces. While such low order models are not completely novel, and Blade Element Momentum theory has been in use for decades, the innovative features of the current work include the ability to model the extreme articulation common in bats and thin lifting surfaces with variable camber, as are observed with compliant membrane wings. In addition, the current model

provides a completely free flight simulation, without any symmetry constraints.

Comparisons between the predictions of blade element momentum theory and the Lagrangian equation of motion show good agreement in the estimation of thrust/drag, and excellent agreement in the prediction of lift. The simulated body trajectories, in reaction to the recorded wing kinematics, demonstrate good agreement with those observed in the live animal experiments.

In addition to providing trajectory simulations, the model will be able to provide critical insight into the forces and torques required for flight (by muscle or servo motor); with further development and in collaboration with more experimental measurements, the model will also provide control derivatives and insight into the requirements for the maintenance of stable flight trajectories of both animals as well as flapping flight robots.

Acknowledgments

This work is supported by a grant from Hyundai Motor Group. Xiaozhou Fan is partially supported by a fellowship from the China Scholarship Council.

References

- [1] Shyy, W., Aono, H., Kang, C.-k., and Liu, H., *An Introduction to Flapping Wing Aerodynamics*, Cambridge University Press, 2013. <https://doi.org/10.1017/cbo9781139583916>.
- [2] Mountcastle, A. M., and Combes, S. A., “Wing flexibility enhances load-lifting capacity in bumblebees,” *Proceedings of the Royal Society B: Biological Sciences*, Vol. 280, No. 1759, 2013. <https://doi.org/10.1098/rspb.2013.0531>.
- [3] Young, J., Walker, S. M., Bomphrey, R. J., Taylor, G. K., and Thomas, A. L. R., “Details of Insect Wing Design and Deformation Enhance Aerodynamic Function and Flight Efficiency,” *Science*, Vol. 325, No. 5947, 2009, pp. 1549–1552. <https://doi.org/10.1126/science.1175928>, URL <http://www.sciencemag.org/cgi/doi/10.1126/science.1175928>.
- [4] Nakata, T., and Liu, H., “Aerodynamic performance of a hovering hawkmoth with flexible wings: A computational approach,” *Proceedings of the Royal Society B: Biological Sciences*, Vol. 279, No. 1729, 2012, pp. 722–731. <https://doi.org/10.1098/rspb.2011.1023>, URL <http://rspb.royalsocietypublishing.org/cgi/doi/10.1098/rspb.2011.1023>.
- [5] Zheng, L., Hedrick, T. L., and Mittal, R., “Time-Varying Wing-Twist Improves Aerodynamic Efficiency of Forward Flight in Butterflies,” *PLoS ONE*, Vol. 8, No. 1, 2013, pp. 1–10. <https://doi.org/10.1371/journal.pone.0053060>.
- [6] Dickinson, M. H., “Wing Rotation and the Aerodynamic Basis of Insect Flight,” *Science*, Vol. 284, No. 5422, 1999, pp. 1954–1960. <https://doi.org/10.1126/science.284.5422.1954>, URL <http://www.sciencemag.org/cgi/doi/10.1126/science.284.5422.1954>.
- [7] Spedding, G. R., Rosén, M., and Hedenström, A., “A family of vortex wakes generated by a thrush nightingale in free flight in a wind tunnel over its entire natural range of flight speeds,” *Journal of Experimental Biology*, Vol. 206, No. 14, 2003, pp. 2313–2344. <https://doi.org/10.1242/jeb.00423>.
- [8] Pennycuik, *Modelling the flying bird*, Academic Press, 2008. <https://doi.org/10.1007/s13398-014-0173-7.2>.
- [9] Parslew, B., and Crowther, W. J., “Simulating avian wingbeat kinematics,” *Journal of Biomechanics*, Vol. 43, No. 16, 2010, pp. 3191–3198. <https://doi.org/10.1016/j.jbiomech.2010.07.024>, URL <http://dx.doi.org/10.1016/j.jbiomech.2010.07.024>.
- [10] Parslew, B., “Predicting power-optimal kinematics of avian wings,” *Journal of the Royal Society Interface*, Vol. 12, No. 102, 2015. <https://doi.org/10.1098/rsif.2014.0953>.
- [11] Riskin, D. K., Bergou, A., Breuer, K. S., and Swartz, S. M., “Upstroke wing flexion and the inertial cost of bat flight,” *Proceedings of the Royal Society B: Biological Sciences*, Vol. 279, No. 1740, 2012, pp. 2945–2950. <https://doi.org/10.1098/rspb.2012.0346>.
- [12] Windes, P., Fan, X., Bender, M., Tafti, D. K., and Müller, R., “A computational investigation of lift generation and power expenditure of Pratt’s roundleaf bat (*Hipposideros pratti*) in forward flight,” *PLoS ONE*, Vol. 13, No. 11, 2018, pp. 1–27. <https://doi.org/10.1371/journal.pone.0207613>.
- [13] Hedenstrom, A., Johansson, L. C., Wolf, M., von Busse, R., Winter, Y., and Spedding, G. R., “Bat Flight Generates Complex Aerodynamic Tracks,” *Science*, Vol. 316, No. 5826, 2007, pp. 894–897. <https://doi.org/10.1126/science.1142281>, URL <http://www.sciencemag.org/cgi/doi/10.1126/science.1142281>.

- [14] Hubel, T. Y., Riskin, D. K., Swartz, S. M., and Breuer, K. S., "Wake structure and wing kinematics: the flight of the lesser dog-faced fruit bat, *Cynopterus brachyotis*," *Journal of Experimental Biology*, Vol. 213, No. 20, 2010, pp. 3427–3440. <https://doi.org/10.1242/jeb.043257>, URL <http://jeb.biologists.org/cgi/doi/10.1242/jeb.043257>.
- [15] Hubel, T. Y., Hristov, N. I., Swartz, S. M., and Breuer, K. S., "Wake structure and kinematics in two insectivorous bats," *Philosophical Transactions of the Royal Society B: Biological Sciences*, Vol. 371, No. 1704, 2016, p. 20150385. <https://doi.org/10.1098/rstb.2015.0385>, URL <http://dx.doi.org/10.1098/rstb.2015.0385%5Cnhttp://rstb.royalsocietypublishing.org/lookup/doi/10.1098/rstb.2015.0385>.
- [16] Viswanath, K., Nagendra, K., Cotter, J., Frauenthal, M., and Tafti, D. K., "Straight-line climbing flight aerodynamics of a fruit bat," *Physics of Fluids*, Vol. 26, No. 2, 2014. <https://doi.org/10.1063/1.4864297>.
- [17] Wang, S., Zhang, X., He, G., and Liu, T., "Numerical simulation of unsteady flows over a slow-flying bat," *Theoretical and Applied Mechanics Letters*, Vol. 5, No. 1, 2015, pp. 5–8. <https://doi.org/10.1016/j.taml.2015.01.006>, URL <http://dx.doi.org/10.1016/j.taml.2015.01.006>.
- [18] Fan, X., Windes, P., Tafti, D., Sekhar, S., Bender, M., Kurdila, A., and Müller, R., "Proper orthogonal decomposition of straight and level flight kinematics in an insectivorous bat," *AIAA Modeling and Simulation Technologies Conference, 2018*, 2018, p. 1. <https://doi.org/10.2514/6.2018-2155>, URL <https://arc.aiaa.org/doi/10.2514/6.2018-2155>.
- [19] Ellington, C. P., "The aerodynamics of hovering insect flight. I. The quasi-steady analysis," *Philosophical Transactions of the Royal Society of London. B, Biological Sciences*, Vol. 305, No. 1122, 1984, pp. 1–15. <https://doi.org/10.1098/rstb.1984.0049>.
- [20] Song, J., Luo, H., and Hedrick, T. L., "Performance of a quasi-steady model for hovering hummingbirds," , 2015. <https://doi.org/10.1016/j.taml.2014.12.003>.
- [21] Vejdani, H. R., Boerma, D. B., Swartz, S. M., and Breuer, K. S., "The dynamics of hovering flight in hummingbirds, insects and bats with implications for aerial robotics," *Bioinspiration and Biomimetics*, Vol. 14, No. 1, 2019. <https://doi.org/10.1088/1748-3190/aaea56>.
- [22] Glauert, H., *The Elements of Aerofoil and Airscrew Theory*, Cambridge University Press, 1983. <https://doi.org/10.1017/CBO9780511574481>, URL <https://www.cambridge.org/core/product/identifier/9780511574481/type/book>.
- [23] OSBORNE, M. F., "Aerodynamics of flapping flight with application to insects." *The Journal of experimental biology*, Vol. 28, No. 2, 1951, pp. 221–245.
- [24] Hedrick, T. L., Usherwood, J. R., and Biewener, A. A., "Low speed maneuvering flight of the rose-breasted cockatoo (*Eolophus roseicapillus*). II. Inertial and aerodynamic reorientation," *Journal of Experimental Biology*, Vol. 210, No. 11, 2007, pp. 1912–1924. <https://doi.org/10.1242/jeb.002063>.
- [25] Clawson, T. S., Fuller, S. B., Wood, R. J., and Ferrari, S., "A blade element approach to modeling aerodynamic flight of an insect-scale robot," *American Control Conference (ACC), 2017*, IEEE, 2017, pp. 2843–2849.
- [26] Pennycuick, C. J., "Power Requirements for Horizontal Flight in the Pigeon *Columba Livia*," *Journal of Experimental Biology*, Vol. 49, No. 3, 1968, pp. 527–555.
- [27] Sekhar, S., Windes, P., Fan, X., and Tafti, D. K., "Canonical description of wing kinematics and dynamics for a straight flying insectivorous bat (*Hipposideros pratti*)," *PLoS ONE*, Vol. 14, No. 6, 2018. <https://doi.org/10.1371/journal.pone.0218672>.
- [28] Kang, C. K., Cranford, J., Sridhar, M. K., Kodali, D., Landrum, D. B., and Slegers, N., "Experimental characterization of a butterfly in climbing flight," *AIAA Journal*, Vol. 56, No. 1, 2018, pp. 15–24. <https://doi.org/10.2514/1.J055360>.
- [29] Gopalakrishnan, P., and Tafti, D. K., "Effect of Wing Flexibility on Lift and Thrust Production in Flapping Flight," *AIAA Journal*, Vol. 48, No. 5, 2010, pp. 865–877. <https://doi.org/10.2514/1.39957>, URL <http://arc.aiaa.org/doi/10.2514/1.39957>.
- [30] Kang, C. K., and Shyy, W., "Analytical model for instantaneous lift and shape deformation of an insect-scale flapping wing in hover," *Journal of the Royal Society Interface*, Vol. 11, No. 101, 2014. <https://doi.org/10.1098/rsif.2014.0933>.
- [31] Thollessen, M., and Norberg, U. M., "Moments of inertia of bat wings and body," *Journal of Experimental Biology*, Vol. 158, 1991, pp. 19–35.
- [32] Whitney, J. P., and Wood, R. J., "Aeromechanics of passive rotation in flapping flight," *Journal of Fluid Mechanics*, Vol. 660, No. July 2010, 2010, pp. 197–220. <https://doi.org/10.1017/S002211201000265X>.

- [33] Cheng, B., and Deng, X., “Translational and rotational damping of flapping flight and its dynamics and stability at hovering,” *IEEE Transactions on Robotics*, Vol. 27, No. 5, 2011, pp. 849–864. <https://doi.org/10.1109/TRO.2011.2156170>.
- [34] Tu, Z., Fei, F., Zhang, J., and Deng, X., “An At-Scale Tailless Flapping-Wing Hummingbird and Experimental Validation,” *IEEE Transactions on Robotics*, Vol. 36, No. 5, 2020, pp. 1–15.
- [35] Riskin, D. K., Willis, D. J., Iriarte-Diaz, J., Hedrick, T. L., Kostandov, M., Chen, J., Laidlaw, D. H., Breuer, K. S., and Swartz, S. M., “Quantifying the complexity of bat wing kinematics,” *Journal of Theoretical Biology*, Vol. 254, No. 3, 2008, pp. 604–615. <https://doi.org/10.1016/j.jtbi.2008.06.011>.
- [36] Folch-Fortuny, A., Arteaga, F., and Ferrer, A., “Missing Data Imputation Toolbox for MATLAB,” *Chemometrics and Intelligent Laboratory Systems*, Vol. 154, 2016, pp. 93–100. <https://doi.org/10.1016/j.chemolab.2016.03.019>, URL <http://dx.doi.org/10.1016/j.chemolab.2016.03.019>.
- [37] Anderson, J. D., *Fundamentals of Aerodynamics*, McGraw-Hill Education, 2010.
- [38] Sane, S. P., and Dickinson, M. H., “The aerodynamic effects of wing rotation and a revised quasi-steady model of flapping flight,” *The Journal of experimental biology*, Vol. 205, No. Pt 8, 2002, pp. 1087–1096. <https://doi.org/10.1126/science.167.3915.177>.
- [39] Fung, Y. C. Y.-c., *An introduction to the theory of aeroelasticity*, Dover Publications, 2008.
- [40] Usherwood, J. R., “The aerodynamic forces and pressure distribution of a revolving pigeon wing,” *Experiments in Fluids*, Vol. 46, No. 5, 2009, pp. 991–1003. <https://doi.org/10.1007/s00348-008-0596-z>.
- [41] Bergou, A. J., Swartz, S. M., Vejdani, H., Riskin, D. K., Reimnitz, L., Taubin, G., and Breuer, K. S., “Falling with Style: Bats Perform Complex Aerial Rotations by Adjusting Wing Inertia,” *PLoS Biology*, Vol. 13, No. 11, 2015, pp. 1–16. <https://doi.org/10.1371/journal.pbio.1002297>.
- [42] Ramezani, A., Shi, X., Chung, S. J., and Hutchinson, S., “Lagrangian modeling and flight control of articulated-winged bat robot,” *IEEE International Conference on Intelligent Robots and Systems*, Vol. 2015-Decem, 2015, pp. 2867–2874. <https://doi.org/10.1109/IROS.2015.7353772>.